JGR Solid Earth

RESEARCH ARTICLE
10.1029/2020JB021271

Effect of Glacial/Interglacial Recharge Conditions on Flow of Meteoric Water Through Deep Orogenic Faults: Insights Into the Geothermal System at Grimsel Pass, Switzerland

Peter Alt-Epping[1], Larryn W. Diamond[1], Christoph Wanner[1], and Glenn E. Hammond[2]

[1]Rock-Water Interaction Group, Institute of Geological Sciences, University of Bern, Bern, Switzerland, [2]Pacific Northwest National Laboratory, Richland, WA, USA

Key Points:

- Gradients in topography can drive meteoric water to depths exceeding 10 km where it acquires temperatures in excess of 250°C
- Recharge limited conditions induce a layered flow system in orogenic faults with shallow single pass flow and deep non-Rayleigh convection
- If the depth of meteoric infiltration is known, a minimum length of the fault plane can be estimated

Correspondence to:
P. Alt-Epping,
alt-epping@geo.unibe.ch

Citation:
Alt-Epping, P., Diamond, L. W., Wanner, C., & Hammond, G. E. (2021). Effect of glacial/interglacial recharge conditions on flow of meteoric water through deep orogenic faults: Insights into the geothermal system at Grimsel Pass, Switzerland. *Journal of Geophysical Research: Solid Earth*, *126*, e2020JB021271. https://doi.org/10.1029/2020JB021271

Received 2 NOV 2020
Accepted 22 JUN 2021

Abstract Many meteoric-recharged, fault-hosted geothermal systems in amagmatic orogenic belts have been active through the Pleistocene glacial/interglacial climate fluctuations. The effects of climate-induced recharge variations on fluid flow patterns and residence times of the thermal waters are complex and may influence how the geothermal and mineralization potential of the systems are evaluated. We report systematic thermal-hydraulic simulations designed to reveal the effects of recharge variations, using a model patterned on the orogenic geothermal system at Grimsel Pass in the Swiss Alps. Previous studies have shown that fault-bounded circulation of meteoric water is driven to depths of ~10 km by the high alpine topography. Simulations suggest that the current single-pass flow is typical of interglacial periods, during which (a) meteoric recharge into the fault is high (above tens of centimeters per year), (b) conditions are at or somewhat below the critical Rayleigh number, and (c) hydraulic connectivity along the fault plane is extensive (an extent of at least 10 km into increasingly higher terrain is required to explain the 10 km penetration depth). The subcritical condition constrains the bulk fault permeability to <1e-14 m^2. In contrast, the limited recharge during the numerous Pleistocene glaciation events likely induced a layered flow system, with single-pass flow confined to shallow depths while non-Rayleigh convection occurred deeper in the fault. The same layering can be observed at low aspect ratios (length/depth) of the fault plane, when the available recharge area limits flux through the fault.

Plain Language Summary Many fault-hosted geothermal systems in mountainous regions have been active through the Pleistocene glacial/interglacial climate fluctuations. As a result of climate change, meteoric recharge into these systems has changed over time, affecting geothermal circulation in the fault and hence influencing the geothermal and mineralization potential of the systems. We present a series thermal-hydraulic simulations designed to reveal the effects of recharge variations, using a model patterned on the orogenic geothermal system at Grimsel Pass in the Swiss Alps. Previous studies have shown that fault-bounded circulation of meteoric water is driven to depths of ~10 km by the high alpine topography. Simulations suggest that the current single-pass flow pattern is typical of interglacial periods, during which (a) meteoric recharge into the fault is high, (b) the contribution of buoyancy as a driving force for fluid flow is low, and (c) hydraulic connectivity along the fault plane is extensive. The deep, single-pass flow pattern constrains the bulk fault permeability to <1e-14 m^2. In contrast, the limited recharge during the numerous Pleistocene glaciation events likely induced a layered flow system, with single-pass flow confined to shallow depths while slow non-Rayleigh convection occurred deeper in the fault.

1. Introduction

Orogenic geothermal systems originate as a consequence of deep faults providing permeable fluid pathways in combination with topography-induced hydraulic head gradients driving flow of meteoric water. Even in orogens without magmatic activity and with low geothermal gradients, thermal fluids have been found discharging at the surface. Examples are in the Canadian Rocky Mountains (Grasby & Hutcheon, 2001; Grasby et al., 2016), the Southern Alps of New Zealand (Menzies et al., 2014; Reyes, 2015; Reyes et al., 2010), the central European Alps (Diamond et al., 2018; Pfeifer et al., 1992; Sonney & Vuataz, 2008, 2009, 2010;

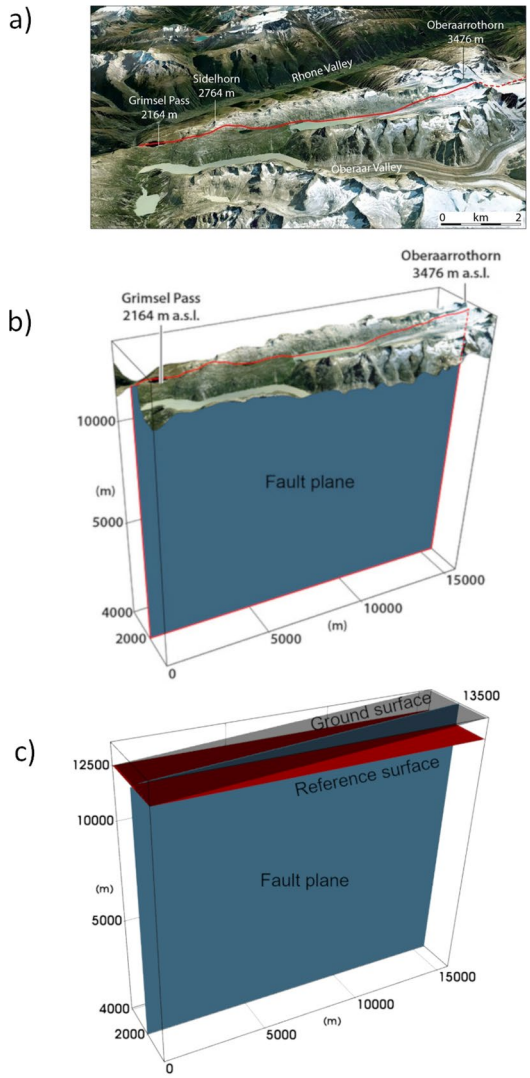

Figure 1. View from the north toward Grimsel Pass and the surrounding mountains. (a) The trace of the Grimsel fault is shown in red. (b) Conceptually, the fault (in blue) is a planar, discrete flow system, extending into increasingly higher terrain from east to west. (c) In the model, a generic topography is added onto a horizontal reference surface (in red). The linear increase in topography along strike of the fault shown here in gray constitutes the base case as described in the text. Without topography the model is a block of dimensions 15.7 × 4.1 × 12.5 km. A vertical, 100 m wide fault plane is sandwiched between two blocks of low permeability rock. The depth of the fault (the distance between bottom and reference surface) is 12.5 km.

Wanner et al., 2019), Taiwan (Upton et al., 2011), the Qilian Mountains of western China (Stober et al., 2016) and the Himalayas (Craw et al., 2005; Hochstein & Yang, 1995).

In this study, numerical modeling is used to explore the dynamics of regional-scale fluid circulation through orogenic geothermal systems that are limited by recharge conditions. Such recharge limitation is typical of orogens affected by repeated glacial and interglacial events during the Pleistocene. To ensure realism we pattern our model loosely on the fault-hosted geothermal system at the Grimsel Pass in the Swiss Alps (Figure 1a). Our model obeys constraints from sampled thermal waters and altered wall rock, as well as climatic, geological and geochemical evidence from the Grimsel Pass region. A more rigorous model of the Grimsel system aimed at matching observations at the discharge site is the topic of a forthcoming study.

During Pleistocene glaciation the Swiss Alps were covered with an ice sheet up to several hundreds of meters thick. Based on the sequence of glacial deposits in the Swiss Molasse Basin, at least eight glacial cycles have been identified (Preusser et al., 2011). Each cycle may have comprised several individual periods of ice build-up and intermittent periods of milder temperatures. Given that the Grimsel recharge zone lay between 2,000 and 3,000 m in altitude, it is reasonable to assume that rainfall and meltwater input into the Grimsel fault system was low during glaciation events (Dzikowski et al., 2016; Maréchal et al., 1999; Thiebaud et al., 2010). However, quantitative details about recharge conditions during the Pleistocene are not available. Here, we use our model to test limiting assumptions on the hydraulic conditions and to hence gain insights into the systematics of deep fault-bounded flow systems subject to fluctuating recharge.

2. The Orogenic Geothermal System at Grimsel Pass, Switzerland

Several low-flow thermal springs discharging water at <10 l/min and at temperatures up to 28°C (Pfeifer et al, 1992; Waber et al., 2017) are present in a N-S trending tunnel hosting a trans-European pipeline for natural gas. The discharge sites in the tunnel lie about 250 m beneath Grimsel Pass, a mountain pass crossing the Bernese Oberland at an elevation of 2,164 m. The thermal springs at Grimsel Pass are the highest known in the Alps (Hofmann et al., 2004). Discharge is confined to a relatively short (<100 m) section of the tunnel where it intersects a major brecciated fault zone which is part of the larger Grimsel Breccia fault (GBF), a late Neogene strike-slip fault dipping steeply at 85° to NNW (Belgrano et al., 2016). The breccia zone of the GBF has a sub-vertical, pipe-like structure in 3D and constitutes a brittle, permeable linkage zone between sub-parallel fault planes of the main shear-zone.

Toward the west of Grimsel Pass the fault extends into progressively higher mountains that reach over 3,500 m a.s.l (Figure 1a). The rocks to the north and south of the GBF are of low permeability, composed of granite or gneisses or low-permeability mylonites associated with the fault. The discharge of the thermal waters at the high pass demonstrates the lack of hydraulic conductivity between the fault zone and the surrounding rocks, which fall away to the north and south into deep NE-SW-trending valleys. The fault thus constitutes a narrow, planar, discrete flow system, extending into increasingly higher terrain from east

to west (Figure 1b). Superimposed on this gradual westward increase in surface elevation are local peaks and troughs, such as the Sidelhorn mountain (2,764 m a.s.l.) some 2 km west of Grimsel Pass (Figure 1a).

Isotope analyses of thermal water sampled in the tunnel reveal the meteoric origin of the water and its infiltration altitude ≥500 m above Grimsel pass. Diamond et al. (2018) estimated a minimum temperature of 211°C for the deep thermal end-member, based on Na/K ratios in the spring water. They argued that the maximum temperature is probably in the range of 230°C–250°C, possibly even higher. Given that there is no additional heat source in the region, the locally estimated geothermal gradient of 25°C/km (Vernon et al., 2008) constrains the depth of circulation to at least 10 km (Diamond et al., 2018; Wanner et al., 2019). This distinct geochemical signature of deep water-rock interaction implies that little geochemical overprinting occurred during ascent of the thermal water. The depletion of ^{14}C in the springs suggests that the thermal water resided in the hydrothermal circulation system for at least 30,000 years (Waber et al., 2017). Geochemical data are therefore consistent with the conceptual model of topography driving a deep-reaching, single-pass flow system. Radiometric dating of alteration minerals shows the system has been active (presumably intermittently) over the past 3.3 Ma (Hofmann et al., 2004).

Because of the high altitude of the Grimsel Pass and the mountains surrounding it, rates of meteoric recharge into the fault probably undergo seasonal variations: rates are low in winter when precipitation falls predominantly as snow and rates are high in summer due to snow melt, rainfall and melting glaciers. However, considering the long residence time of the hydrothermal fluid in the flow system, transient recharge conditions related to climate variations on time scales of tens of thousands of years are likely to have determined the flow regime in the fault. It can be expected that during peak glaciation in the Pleistocene, precipitation at high altitude occurred predominantly as snow and the influx of liquid water into the fault was at a minimum, thereby limiting the total flux through the geothermal system. During interglacial periods the influx of liquid water increased when snow and ice melted and precipitation occurred as rain during the warm months of the year. These periods constituted a return to an excess supply of meteoric water, such that the rate of infiltration was controlled by the permeability of the fault and by the topography around the recharge zone.

At elevations above about 2,500 m, the permeability of the superficial rock mass may be affected by permafrost where permanent ice partially fills pores and flow channels. The occurrence and depth of permafrost in the Swiss Alps is controlled by the mean ground surface temperature, which is affected by solar radiation, the depth and duration of snow cover, and the geothermal gradient. The depth of permafrost in the Swiss Alps ranges from a few tens of meters to hundreds of meters in the highest terrain. Given the steep and complex Alpine topography and changes in climatic conditions, the distribution of ground surface temperatures and hence of regions affected by permafrost varies in space and time (Noetzli & Phillips, 2019).

Not all water in the permafrost interval is frozen and a fraction of liquid water remains even at temperatures well below zero. The amount of continuous, unfrozen water depends on temperature and to a lesser degree on pressure, water salinity, the mineralogy and the specific surface area of the soil mineral grains (Anderson & Tice, 1972; Anderson & Morgenstern, 1973; Dillon & Andersland, 1966). Silt and clay sediments in particular are prone to remain liquid-water-wet in the presence of ice (Kleinberg & Griffin, 2005). In the Swiss Alps, notable subsurface flow has been demonstrated in permafrost above 2,700 m a.s.l. by Wanner et al. (2018).

There is still considerable uncertainty concerning the effect of permafrost on groundwater flow paths and surface runoff in the Alps, but, aside from introducing heterogeneity, it is not likely to inhibit meteoric infiltration and deep groundwater flow.

3. Model Description

3.1. Previous Work

Convective circulation through faults has been long known as an important mechanism for transporting mass and heat over large distances. Permeable faults are often associated with hydrothermal alteration, ore formation and upwelling thermal waters (e.g., Alt-Epping & Zhao, 2010; Forster & Smith, 1988a, 1988b, 1989; López & Smith, 1995; Magri et al., 2016; Mailloux et al., 1999; Pepin et al., 2014; Simms & Garven, 2004;

Taillefer et al., 2017, 2018; Yang et al., 2004). Convection may occur in three modes: (a) buoyancy-driven convection, also known as free or Rayleigh convection, (a) non-Rayleigh convection, and (c) convection driven by pressure gradients, also known as forced convection. Lapwood (1948) and later Elder (1967) investigated the stability of a saturated porous medium heated uniformly from below and the conditions for the onset of free convection. The vigor of free convection in a porous medium under a uniform geothermal gradient can be described mathematically by the dimensionless Rayleigh number *Ra*, which denotes the ratio of the time scale for diffusive heat transport to the time scale for convective heat transport. The onset of free convection occurs when the critical Rayleigh number is exceeded.

For porous media the Rayleigh number can be written as (e.g., Zhao et al., 2003)

$$Ra = \frac{\left(\rho C_p\right)\rho\alpha\Delta T k z g}{\mu\lambda^e} \tag{1}$$

where z is the thickness of the system, ρ is the average mass density of the fluid, k is the permeability of the porous medium, g is acceleration due to gravity, μ and C_p are the dynamic viscosity and specific heat capacity of the fluid, α is the thermal expansion coefficient, λ^e is the effective thermal conductivity and ΔT is the temperature difference through z. The critical Rayleigh number is system specific and depends on the physical properties of the medium, the properties of the fluid and the thermal and hydraulic boundary conditions imposed on the system.

A second type of convection occurs as a consequence of lateral temperature differences caused by variations of thermal properties, heat flow or topography. This type of convection has been referred to as non-Rayleigh convection (e.g., Wangen, 1997). Non-Rayleigh convection ensuing from lateral temperature gradients due to surface topography only arises in subcritical systems dominated by heat conduction. This implies that non-Rayleigh convection is generally weaker than free Rayleigh convection. For the onset of non-Rayleigh flow there is no critical condition that needs to be overcome. Lateral temperature differences will inevitably result in fluid motion, even at low permeabilities. Although non-Rayleigh convection is generally slow, mass fluxes can exceed those of diffusion such that significant mass transport and chemical fluid-rock reactions are possible over geological time scales. In subcritical convective systems the disparity between conduction-dominated heat transport and advection-dominated solute transport is a reflection of the fact that flow rates required for significant advective transport of solute mass are 1,000–100,000 times lower than those required for significant advection of heat (Bickle & McKenzie, 1987; Ingebritsen et al., 2006).

A third type of convection is forced convection due to topographic relief where groundwater flow is driven by gravity in accord with differences in elevation between recharge and discharge zones. The role of topography-driven flow as an important heat transfer process is often invoked as the cause for anomalous geothermal gradients that cannot be explained by conduction alone (e.g., Smith & Chapman, 1985, and references therein).

These three fluid-flow processes described above (free, non-Rayleigh, and forced convection) are not mutually exclusive. Surface topography, heterogeneities in the rock and/or perturbations inducing transient conditions may cause a combination of these processes to occur to varying extents, at different times or in different parts of the same system. For instance, in mountainous terrain mixed flow systems may evolve when topography-driven flow is imposed on free convection (e.g., Cserepes & Lenkey, 2004; Raffensperger & Vlassopoulos, 1999; Szijárto et al., 2019; Yang et al., 2010). Thus, a given flow pattern, if not controlled by the permeability distribution (i.e., assuming homogeneous conditions), reflects the balance of forces driving these different modes of flow.

3.2. Model Domain and Parameterization

Our numerical model represents the Grimsel fault as a permeable, vertical 100 m wide fault plane sandwiched between two equally sized blocks of low-permeability host rock (Figure 1c). Without topography (i.e., with a flat reference surface, Figure 1c) the model domain is a 3D block with the following dimensions: length 15.7 km, depth 12.5 km, and width 4.1 km. We consider flow deeper than 12.5 km unlikely, as this would be beyond the 310°C transition to purely ductile fault rheology in the quartz-rich host granites and

Table 1
Material Properties

	Fault	Basement rock
Permeability (m^2)	1e-15–1e-14 m^2	3e-20 m^2
Porosity	0.04	0.01
Thermal conductivity (W/[K·m])	3.34	3.34
Heat capacity (J/[K. kg])	800	800
Van Genuchten *alpha* (1/Pa)	1e-4	1e-4
Van Genuchten *m*	0.5	0.5

gneisses (Stöckhert et al., 1999). Topographic relief is added on top of the surface of this block so that the elevation of the model surface is defined by the reference surface plus topographic relief (Figure 1c).

Calculations are performed for different bulk fault permeabilities. It is well known that permeabilities less than 1e-16 m^2 yield conduction-dominated solutions for most plausible upper-crustal conditions (e.g., Manning & Ingebritsen, 1999; Norton & Knight, 1977). Here we use a fault permeability of 1e-15 m^2 as a lower bound, based on insights from an ongoing numerical study in which the fault permeability was calibrated to match discharge rates and temperatures at Grimsel Pass. To allow the role of fluctuating recharge conditions to be easily recognized, we assume a homogeneous permeability distribution throughout the fault and ignore any depth dependency of the permeability distribution or the possibility of preferential flowpaths originating from heterogeneities. For the same reason we also do not consider the observed permeable linkage zones at Grimsel, which clearly act as preferential vertical fluid pathways.

The permeability of the surrounding rock is assumed to be 3e-20 m^2, which corresponds to the measured matrix permeability of the granitic rock hosting the fault (Ota et al., 2003) and which ensures heat transport through the rock is purely conductive. The actual bulk permeability, which includes fractures and micro-fractures, could be as high as 1e-17 m^2 (Wanner et al., 2020). In additional simulations we confirmed that a rock permeability as high as 1e-17 m^2 has little effect on the results. Porosities for the matrix and the fault are 0.01 (Bossart & Mazurek, 1991) and 0.04 (Wanner et al., 2019), respectively. Other material properties are consistent with those used by Wanner et al. (2019) and are summarized in Table 1.

A constant heat flux is assumed along the bottom boundary, resulting in a geothermal gradient of 25°C/km under conductive conditions. In additional simulations, we tested the sensitivity of the results to different conditions for the bottom boundary. This revealed only small differences in temperature, minor differences in flow velocities, and little effect on the general flow pattern. For instance, we tested a 500 m thick conductive bottom layer (representing the ductile lower crust) in combination with a constant, uniform temperature along the bottom boundary. Using a model geometry as in Figure 1c with a linear slope in topography of 0.064 and a fault permeability of 1e-14 m^2, we obtained the same general flow pattern and temperature differences of around 3°C (or 1.1%–1.6%) at a depth of 10 km as for the uniform heat flow case. Hence, the choice of the bottom boundary condition does not significantly impact the results.

The temperature along the surface is fixed at 5°C. We ignore the fact that the air temperature changes with altitude, because the thermal gradient in air is much lower than the geothermal gradient (the adiabatic lapse rate amounts to about 5.5°C/km). We also ignore the fact that the average air temperature may have changed during glacial and interglacial periods.

All side boundaries are impermeable and adiabatic. The model domain can thus be imagined as a discrete, hydraulically active segment of a longer fault plane. The impermeable boundaries at the ends of the segment could then represent offsets of the fracture plane or low-permeability materials clogging fluid pathways.

A common approach to modeling groundwater flow in mountainous terrains is to assume that the water table constitutes the upper boundary of the flow domain. The limitation of this approach is that the magnitude and spatial distribution of meteoric recharge is imposed implicitly. Hence it is not possible to model transient recharge conditions ranging from "zero" to excess recharge, as these require explicit control of the fluid flux across the upper model boundary. This limitation particularly impacts results if the rock is permeable (e.g., Forster & Smith, 1988b, 1989). Therefore, we simulate the elevation of the water table as a function of the infiltration rate explicitly by using a combined flux/conductance boundary condition. This boundary condition will be described in greater detail in the next section.

The initial condition is defined to be hydrostatic and conductive in terms of pressure and temperature, respectively. All simulations are run to 200,000 years. Maintaining all boundary conditions unchanged, this is sufficiently long to ensure that the system is at or near steady state.

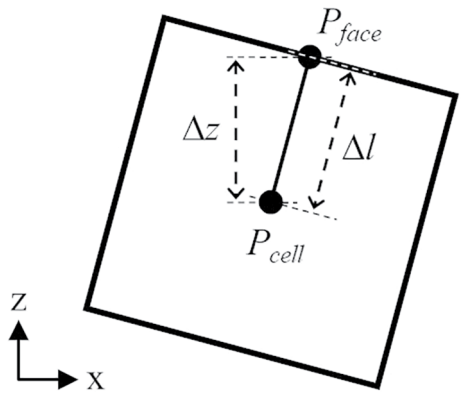

Figure 2. Schematic of conductance boundary condition where Δl is the distance between the cell center and boundary face and Δz is the change in elevation.

3.3. Numerical Model

We use the open source, massively parallel subsurface flow and reactive transport code PFLOTRAN (Hammond & Lichtner, 2010; Hammond et al., 2014; www.pflotran.org) to carry out the flow and heat transport simulations presented here. Because conditions are non-isothermal, Darcy's law can be written as

$$q = -\frac{k}{\mu}\left(\nabla P - \rho g\right) \tag{2}$$

where q is the Darcy flux in m/s, k is the permeability (m^2), μ is dynamic viscosity (Pa·s or kg m^{-1} s^{-1}), ρ is density (kg/m^3), g is gravity (m/s^{-2}), and P is fluid pressure (Pa). PFLOTRAN incorporates equations of state for water that consider temperature- and pressure-dependent density and viscosity. Note that our analysis neglects the conversion of gravitational potential energy to heat as described in Manga and Kirchner (2004).

To simulate the elevation of the water table as a function of meteoric recharge, two boundary conditions are superimposed at the land surface. The first is a Neumann (specified flux) boundary condition that allows infiltration due to precipitation. The second is a conductance boundary condition that discharges excess infiltration once the surface grid cells become saturated.

PFLOTRAN's conductance boundary condition is a specialized Dirichlet (specified pressure) boundary condition that incorporates seepage face criteria and a conductance parameter (Hammond & Lichtner, 2010). The conductance boundary condition employs a modified version of Equation 2 to calculate the flux across the upper boundary according to:

$$q = \frac{C}{\mu}\left(P_{\text{cell}} - P_{\text{face}} + \rho g \Delta z\right) \tag{3}$$

where

$$C = \frac{k}{\Delta l} \tag{4}$$

Here, C is the conductance coefficient (m), P_{cell} and P_{face} are the water pressure at the node and the boundary face, respectively (Pa), and Δl and Δz are the distance and change in elevation between the boundary face and the node of the cell closest to the surface, respectively (m) as illustrated in Figure 2.

Assuming the reference pressure P_{ref} to be atmospheric pressure and saturated conditions, the criteria for defining recharge and discharge areas are as follows:

1. No Inflow: $P_{\text{cell}} \leq P_{\text{face}} + \rho g \Delta z$ and $P_{\text{face}} \leq P_{\text{ref}}$
2. Recharge (inflow): $P_{\text{cell}} < P_{\text{face}} + \rho g \Delta z$ and $P_{\text{face}} > P_{\text{ref}}$
3. Discharge (outflow): $P_{\text{cell}} > P_{\text{face}} + \rho g \Delta z$

Thus, the conductance boundary condition may only discharge or generate no flow if P_{face} is set to P_{ref}. Discharge is facilitated by assigning a relatively large conductance coefficient of 1e-13 m.

These boundary conditions ensure that excess water is treated as runoff when the available recharge exceeds the maximum possible infiltration. Conceptually, this sub-grid cell permeable surface layer associated with a conductance boundary represents unconsolidated alluvial deposits or enhanced weathering or fracturing of the bedrock near the surface.

4. Model Results

4.1. Stability Analysis

Given a model depth of 12.5 km, a temperature difference under conductive conditions of $\Delta T = 312.5$ °C and assuming permeabilities of $k = 1e\text{-}15$ m^2 and $k = 1e\text{-}14$ m^2, the Rayleigh number according to Equation 1 is about 9.8 and 98, respectively. The critical Rayleigh number for an infinitely long porous medium heated uniformly from below and sealed at the top according to Lapwood (1948) ($Ra = 4\pi^2 \approx 39.48$) falls between those values. Murphy (1979) found that the critical Rayleigh number for spontaneous convection in fault hosted systems is orders of magnitude higher than in horizontal porous layers because of the thermal buffering and stabilizing effect of heat transferred to and from the rocks on either side of the fault plane. However, the critical Rayleigh number declines with time as the rock develops a thermal skin, effectively turning the wall rock into an insulator. As a result, the onset of convection in the fault may be delayed. Hence, it can be predicted that, when fluid flow is driven by buoyancy forces alone, conditions at the lower permeability value of 1e-15 m^2 most likely remain conductive, while at a higher permeability of 1e-14 m^2 convective circulation may be initiated during the simulated time period of 200,000 years.

To verify this assessment, numerical simulations were carried out using the reference surface as the top model boundary (Figure 3). All boundaries of the model are impermeable while thermal conditions are as described above. All results represent steady state conditions.

When fault permeability is 1e-15 m^2 the flow field is in motionless equilibrium and heat transport is purely conductive, confirming the assessment based on the Rayleigh number from above. Increasing the permeability to 1e-14 m^2 results in weak convection involving two cells (Figure 3a), indicating that the system has become internally unstable. However, flow velocities are too slow to perturb the conductive temperature field. Increasing the permeability only slightly to 1.5e-14 m^2 results in a stable convection pattern involving four cells (Figure 3b). Although the permeability increases only by a factor of 1.5, the flow velocities increase by several orders of magnitude. However, despite more vigorous flow, heat transport remains primarily conductive. Increasing the permeability to 1e-13 m^2 leads to a vigorously convecting system comprising multiple cells with flow velocities on the order of several m/yr and to convection-controlled heat transport (Figure 3c). The results show that the critical permeability for the onset of free cellular convection is around 1e-14 m^2. The results also demonstrate that, within a span of less than two orders of magnitude in permeability, the flow system changes from motionless to vigorously convective, and the dominant heat transport process changes from conductive to convective. At conditions near the critical Rayleigh number, there is a narrow range of permeabilities over which free convective circulation is initiated but flow is too weak to affect conduction-dominated heat transport.

Similar simulations were carried out for unconfined conditions involving a fixed atmospheric pressure along the top boundary, yielding the same conclusion that the critical permeability for the onset of free convection is around 1e-14 m^2. Note that in the following discussion any reference to the Rayleigh number refers to conditions presented in this section; that is, to conditions without pressure forcing due to topography.

4.2. Effect of Recharge Rate on Hydrothermal Circulation in the Fault Plane-Base Case Topography

The topography between the recharge and discharge regions of the Grimsel fault can be idealized as a linear increase in elevation along strike of the fault (Figure 1c). A linear increase in surface elevation from left to right with a total difference in height $dh = 1{,}000$ m, yielding a hydraulic gradient of 6.4e-2, is defined as the base case topography. This case is compared with other configurations of topographic highs and lows in Figure 4a. Additional simulations using different peak elevations (dh) to assess the effect of the topographic slope are also carried out.

4.2.1. Excess Recharge Conditions

Excess recharge occurs when the supply of meteoric water (e.g., from rainfall and/or meltwater) exceeds the infiltration capacity of the fault, thereby resulting in surface runoff. The rock is fully saturated and the water table coincides with the ground surface (Figure 4b). Under these conditions and using a fault permeability of 1e-15 m^2, the steady state flow pattern is a single-pass flow-through system (Figure 5a), consistent

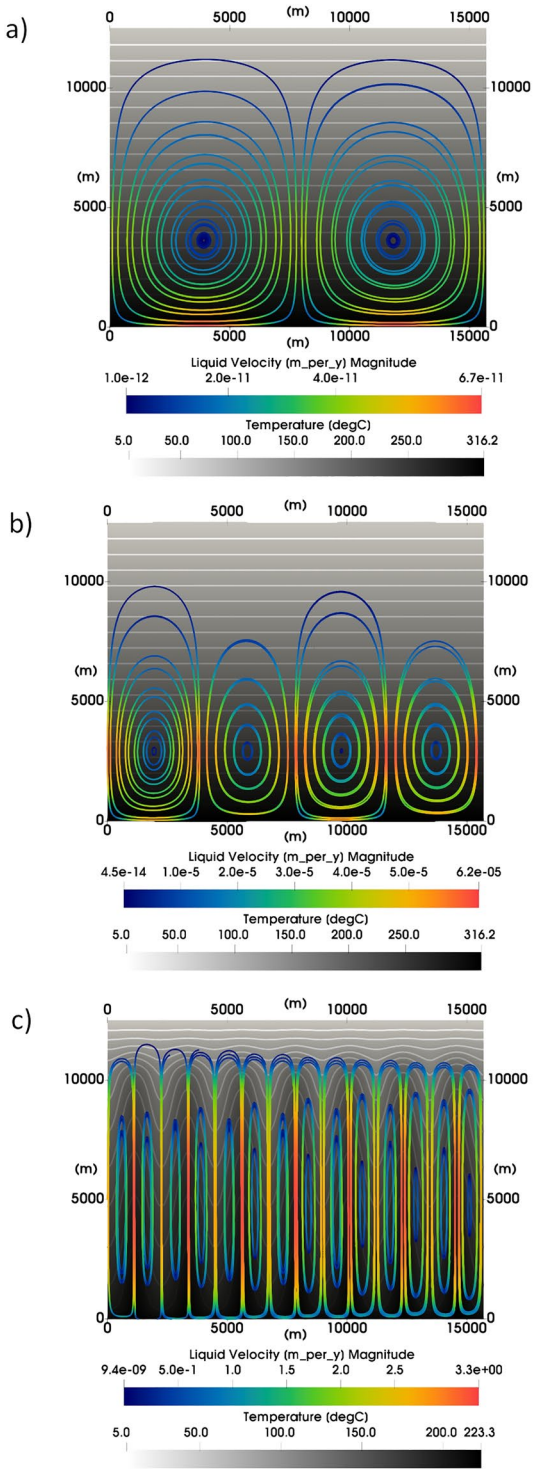

Figure 3. Stability analysis for the Grimsel fault model without topography. The plots show colored streamlines overlying isotherms (grayscale contours). (a) The critical permeability for the onset of free convection is around 1e-14 m^2. The convection pattern consists of two cells with very low flow velocities. (b) Increasing the permeability slightly to 1.5e-14 m^2 changes the convection pattern into multiple cells and the vigor of convection increases by several orders of magnitude. Heat transport is still primarily conductive. (c) At even higher permeabilities (1e-13 m^2) convection becomes vigorous, multiple convection cells extend over the entire vertical length of the domain, and heat transport is controlled by convection.

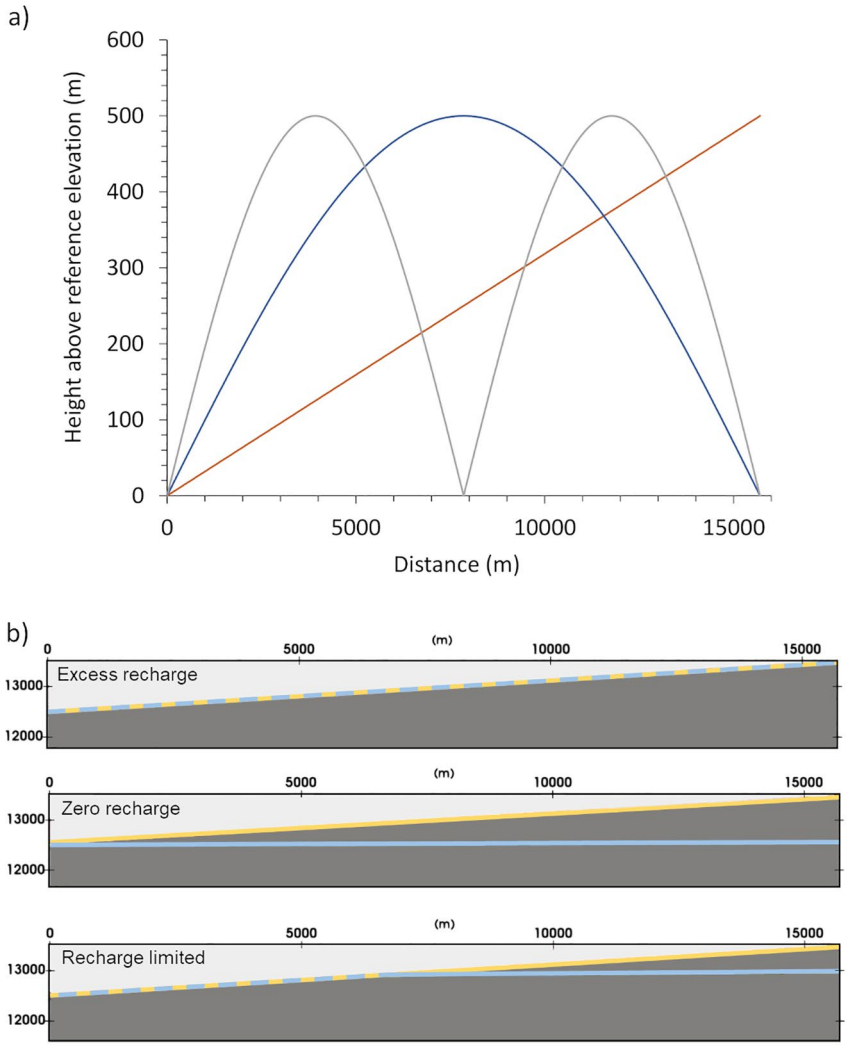

Figure 4. (a) Three alternative generic topographies along strike of the fault (here with dh = 500 m), stacked on top of the 12.5 km deep model domain: a linear increase in height (brown) considered as the base case, a single peak in the center (blue) and two peaks (gray). (b) Configuration of the base case surface topography (yellow line) and water table (blue line) depending on recharge conditions: excess recharge, zero recharge and recharge-limited infiltration.

with what has been conceptually envisaged for the Grimsel system. The entire fault plane is affected by topography-driven flow, and meteoric water penetrates to the bottom of the fault plane, attaining temperatures of up to 335°C. Highest flow rates are on the order of several centimeters per year and occur at the far ends of the domain where the impermeable side boundaries impose a barrier to flow, thereby funneling up- and downflow. The single-pass flow pattern is reminiscent of the 2D "Unit Basin" model described by Tóth (2009) in which basinal flow is driven solely by gravity. As in Tóth (2009), the hydraulic gradient and the flow intensity decrease with depth. The higher the point of recharge, the deeper the flowline and the longer the flowpath and residence time (Figure 5a). In other words, the recharge elevation of a given aliquot of water correlates with its highest attained temperature and with its residence time in the system. Heat transport is predominantly conductive as the isotherms follow the slope of the ground surface. Isotherms are slightly deflected upward in the zone of strongest fluid upflow near the left boundary of the domain, due to the convective heat transport (Figure 5a). Monitoring the temperature at an arbitrary point in this zone of fluid upflow positioned at 250 m from the left boundary (x = 250 m), and at a shallow depth of 265 m below surface (a depth comparable to that of the tunnel below Grimsel Pass) reveals a temperature increase of about 2°C compared to purely conductive conditions.

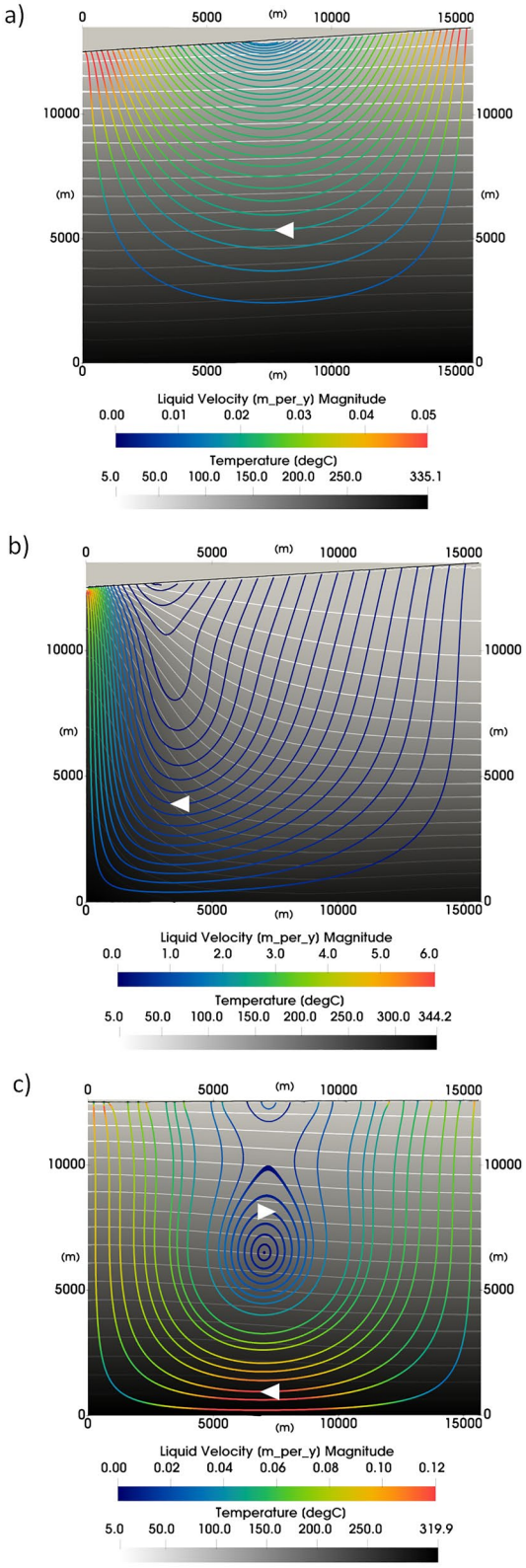
a)
0
5000
(m)
10000
15000
10000
(m)
5000
0
Liquid Velocity (m_per_y) Magnitude
0.00 0.01 0.02 0.03 0.04 0.05
Temperature (degC)
5.0 50.0 100.0 150.0 200.0 250.0 335.1
b)
Liquid Velocity (m_per_y) Magnitude
0.0 1.0 2.0 3.0 4.0 5.0 6.0
Temperature (degC)
5.0 50.0 100.0 150.0 200.0 250.0 300.0 344.2
c)
Liquid Velocity (m_per_y) Magnitude
0.00 0.02 0.04 0.06 0.08 0.10 0.12
Temperature (degC)
5.0 50.0 100.0 150.0 200.0 250.0 319.9

Figure 5

By reducing the topographic gradient (i.e., by lowering dh), the hydraulic gradient is also reduced. This lowers the fluxes through the fault but the single-pass flow pattern remains stable down to very low hydraulic gradients (the lowest gradient tested is 6.4e-3).

Increasing the permeability to 1e-14 m^2 results in a single-pass flow system overprinted by buoyancy forces (Figure 5b). Heat transport is dominated by convective flow, in particular in the zone of fluid upflow. Compared to conduction-dominated conditions (Figure 5a), the flow field is more asymmetric, with focused upflow of hot water at velocities of several m/yr and a broad zone of diffuse recharge where flow velocities are generally less than 0.5 m/yr. The reasons for this asymmetry are feedbacks between temperature and the fluid properties viscosity and density in the zone of fluid upflow. Both viscosity and density are lower in the high temperature fluid ascending from depth than in the cold fluid descending into the plane, leading to "self-channeling" of fluid upflow. In contrast, the recharge zone broadens, rendering meteoric infiltration more diffuse.

Decreasing the hydraulic gradient to 6.4e-3 (dh = 100 m) reduces the topographic forcing and enhances the effect of buoyancy on the pattern of flow. A small convection cell forms in the center of the fault plane (Figure 5c). The convection cell is surrounded by a single-pass flow system with flow velocities on the order of 0.1 m/year. Single-pass flow is strong enough to affect the slope of the isotherms in the recharge and discharge zones. The convection cell forms at the inflection point of the isotherms where the steepest temperature gradients occur.

Because of higher density contrasts between up- and down-flow, the vertical flow component is stronger than under conductive conditions. That is, more water penetrates into the deeper and hotter region of the fault plane, which has thermal as well as geochemical implications for the water discharging at the surface (Figures 5b and 5c). The water ascending from depth moves faster, and hence carries more thermal energy and is more likely to show evidence of high-temperature fluid-rock interaction. At the same location (x = 250 m, 265 m below the surface) the temperature of the upwelling fluid is about 155°C higher than at a fault permeability of 1e-15 m^2 (Figure 5b).

If the permeability is increased to 1e-13 m^2, free convection completely dominates the flow pattern in the fault plane and confines topography-driven single-pass flow to shallow depths. Thus, deep single-pass flow systems such as at Grimsel Pass can only operate at conditions at or below the critical Rayleigh number. This implies that there is an upper limit for the permeability of the Grimsel fault above which deep single-pass flow is no longer possible. In our model representation of the Grimsel system, this upper limit is on the order of 1e-14 m^2. This insight reduces the range of realistic bulk fault permeabilities to roughly one order of magnitude, that is between 1e-15 m^2 and 1e-14 m^2.

4.2.2. Zero Recharge Conditions

Assuming zero recharge is an extreme condition that may have never occurred, even during periods of peak glaciation. It is presented here in Figures 6a and 6b as a limiting case. Without recharge the water table is flat and there is no pressure forcing due to topography (Figure 4b). When fault permeability is 1e-15 m^2, flow is driven solely by non-Rayleigh convection, due to the higher temperature attained under the topographic high. The stable flow pattern consists of a single large convection cell with upflow under the topographic high and downflow under the topographic low. This pattern is reminiscent of circulation in sub-seafloor convection systems where off-axis fluid flow is controlled by the same features: no water-table relief, and hotter conditions under topographic highs (Fisher et al., 1990). Compared to the single-pass flow

Figure 5. Flowfield as streamlines and temperature distribution after 200 kyr. The flow direction is indicated by white arrowheads. (a) For a fault permeability of 1e-15 m^2, a topographic gradient of 6.4e-2 (1,000 m increase in altitude from left to right) and excess available recharge, a single-pass flow system arises in which flow is driven by head gradients induced by the topography. Highest flow velocities are on the order of cm/yr and decrease to less than 1 mm/yr in the deep plane. Flow velocities are too slow to perturb the conductive temperature field, except in the shallow upflow zone. (b) Increasing the fault permeability to 1e-14 m^2 and using the same topographic gradient of 6.4e-2 results in convection-dominated heat transport. The lower viscosity and higher mobility of the fluid at higher temperatures promotes focused discharge while the area of the recharge expands and infiltration becomes more diffuse. (c) Using the same permeability (1e-14 m^2) but a lower topographic gradient of 6.4e-3 (dh = 100 m) decreases pressure forcing and enhances buoyancy as the driving force for flow. The flow field is more symmetrical than in (b), exhibiting a central convection cell surrounded by deep single-pass flow. Note the relatively high flow velocities in the deep fault.

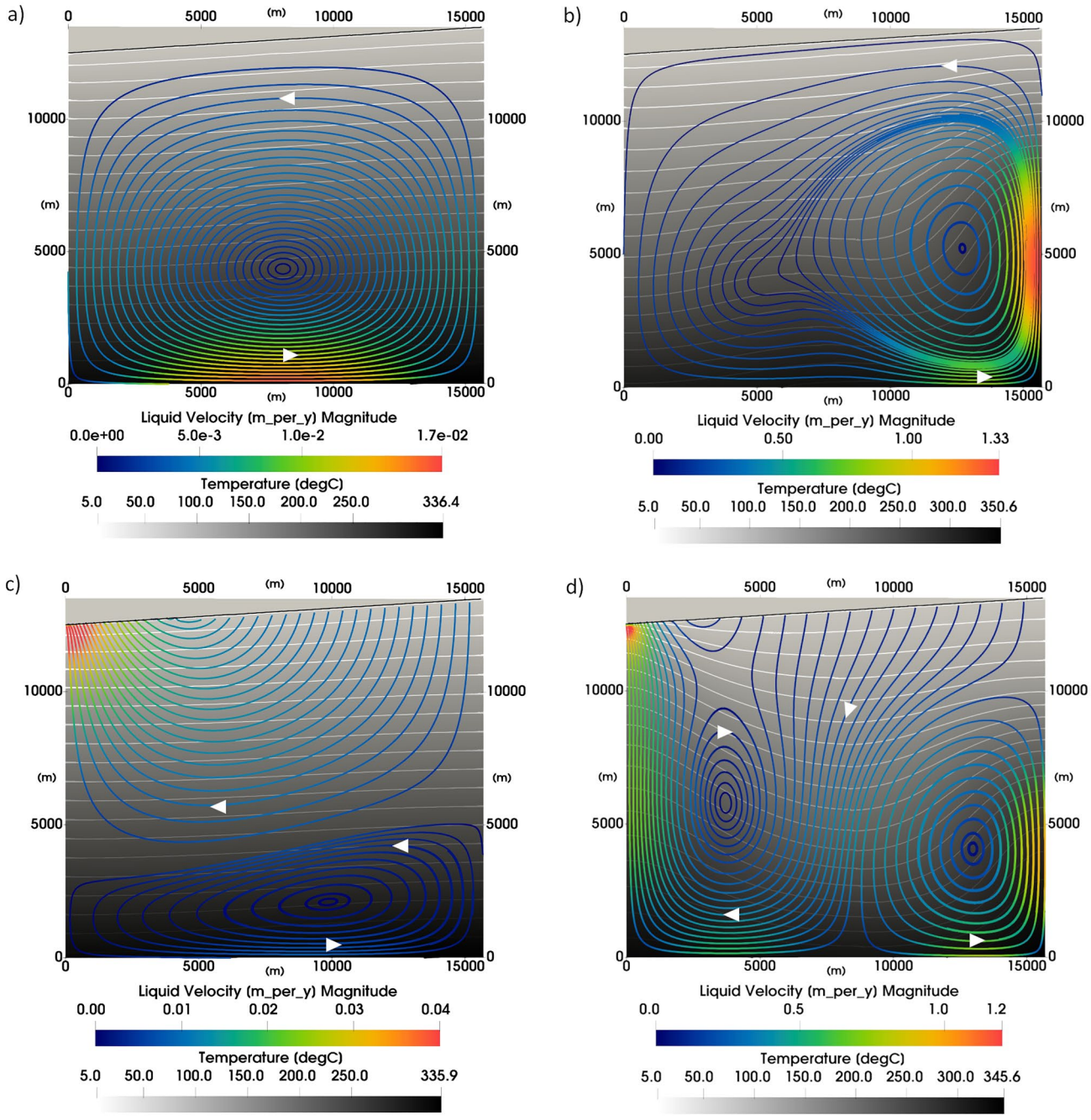

Figure 6. (a and b) Closing the top boundary to recharge results in a single large convection cell that rotates in a counter clockwise direction. Flow is driven by thermal gradients imposed by the surface topography. Up- and down-welling occurs under topographic highs and lows, respectively. White arrowhead indicates flow direction. (a) Case where permeability and topographic gradient are 1e-15 m^2 and 6.4e-2, respectively. (b) Increasing the permeability to 1e-14 m^2 at zero recharge leads to a distorted single convection cell. Upflow is confined to a roughly 3,000 m wide zone in the right half of the domain (under high surface elevation). Flow velocities are relatively high due to feedbacks between temperature and fluid properties (highest flow velocities are around 1.0 m/yr in the upflow zone). Focused upflow is balanced by broad, diffuse downflow toward the left of the domain. (c and d) Recharge-limited conditions result in mixed flow systems involving single-pass flow and convection. Weak lateral temperature gradients induced by the topography initiate slow convective circulation in the deep fault. (c) Using a fault permeability of 1e-15 m^2, a topographic gradient of 6.4e-2 and an infiltration rate of 0.01 m/yr, the amount of infiltrating meteoric water is no longer sufficient to penetrate to the bottom of the fault and a layered flow system evolves. (d) Increasing the permeability to 1e-14 m^2 and using an infiltration rate of 0.1 m/yr, two convection cells form, confining single-pass flow through the bottom of the fault to a narrow zone between them.

system in Figure 5a, the flow direction in the deep fault is reversed. Flow velocities for dh = 1,000 are on the order of 1e-2 m/yr in the deep fault and around 1e-3 m/yr at shallow depths (Figure 6a). A more gentle slope (e.g., dh = 100 m) decreases the flow velocities by roughly one order of magnitude, while the general flow pattern of a single large convection cell remains unchanged.

Increasing the permeability to 1e-14 m^2 introduces buoyant instabilities (Figure 6b), perturbing the symmetry of the single convection cell seen in Figure 6a. Relatively high flow velocities in the upflow zone bend isotherms upwards, which in turn feeds back into temperature-dependent fluid properties in the ascending water, thereby inducing "self-channeling" as in Figure 5b, but below the topographic high.

4.2.3. Recharge Limited Conditions

If recharge of meteoric water is non-zero but lower than the infiltration capacity of the fault zone, an unsaturated zone develops in the shallow subsurface and flow through the fault plane is limited by the supply of meteoric water (Figure 4c). The groundwater table falls below the surface at high altitude, decreasing the hydraulic gradient and the topography-driven fluxes through the fault. As a consequence, buoyancy forces become increasingly important in controlling the pattern of flow. Because the flow intensity decreases with depth (Tóth, 2009), this change in the predominant flow process first becomes apparent in the deep fault.

When fault permeability is 1e-15 m^2, a recharge rate below 0.016 m/yr leads to collapse of the single-pass flow system into a layered system with topography-driven flow confined to shallow depths and non-Rayleigh convection in the deep fault (Figure 6c). The depth of the transition between the two flow regimes is determined by the balance of two opposing forces, gravity and buoyancy. Flow velocities within the shallow single-pass flow region of the fault plane are generally higher than in the deep convection cell, where Darcy flow velocities are only on the order of millimeters per year (Figure 6c). Reducing meteoric infiltration further, buoyancy-driven flow expands at the expense of single-pass flow until, at zero recharge, the flow system comprises a single convection cell as in Figure 5a.

At higher fault permeabilities larger infiltration rates are needed to sustain a stable, deep single-pass flow system because free convection competes more effectively with pressure-driven flow. When fault permeability is 1e-14 m^2, the critical infiltration rate needed to sustain single-pass flow to the bottom of the fault plane is about 0.3 m/yr. This is almost a factor of 20 higher than the infiltration rate required at a fault permeability of 1e-15 m^2. When the infiltration rate falls below this threshold, free convection initiates under the topographic high in the bottom right corner of the fault plane. A mixed flow system arises in which single-pass flow is confined to regions not affected by cellular convection. This can lead to instances in which single-pass flow is channeled in narrow zones between convection cells (Figure 6d). The flow pattern is difficult to predict as it is governed by the arrangement of convection cells. At infiltration rates below about 0.02 m/yr the infiltrating water no longer penetrates to the bottom of the fault. A layered flow system arises in which a single large convection cell at depth is overlain by shallow single-pass groundwater flow.

4.2.4. Transient Conditions

So far we have examined steady state flow patterns resulting from different (constant) recharge conditions. Evidence from glacial deposits suggests that at least 8 glacial cycles occurred during the Quaternary when glaciers extended into the lowlands of northern Switzerland (Preusser et al., 2011). The duration of these events can be on the order of several tens of thousands of years. The question arises as to how quickly the flow pattern in the fault responds to changes in recharge conditions. To answer this question we run a simulation with excess recharge conditions to steady state using a permeability of 1e-15 m^2. Then we start alternating between excess and zero recharge using progressively longer time intervals and monitor the response of the system.

Results show that the system is very responsive to changes in recharge conditions (Figure 7). Even over the shortest assumed time interval of 1,000 years, the flow system collapses into a layered flow system when recharge ceases during glaciation and is restored to a single-pass system when excess recharge conditions return during an interglacial period. This alternating flow pattern coincides with a reversal in the flow direction in the deep fault (z = 1,000 m; Figure 7a). During glaciation the deep convection cell grows continuously and conditions remain transient, while the system changes abruptly to steady single-pass flow at the transition to interglacial periods.

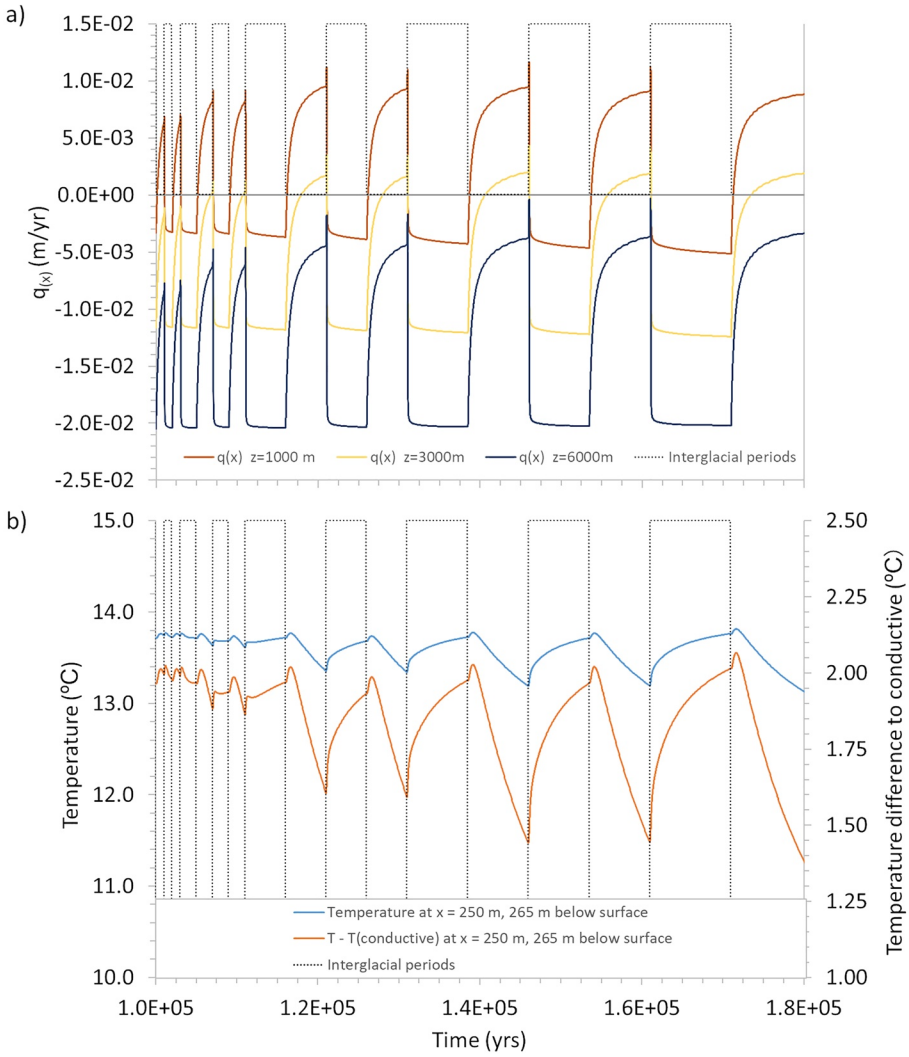

Figure 7. Simulation of transient recharge conditions involving alternating glacial (zero recharge) and interglacial (excess recharge) periods of increasing duration. (a) The velocity component in the horizontal direction ($q_{(x)}$) at $x = 12{,}500$ m and for different depths z (zero is bottom of the domain) is shown to visualize the response of the flow field. If $q_{(x)} < 0$, flow is from right to left. If $q_{(x)} > 0$ flow is from left to right. In the deep fault (e.g., $z = 1{,}000$ m), alternating single-pass flow and non-Rayleigh convection are marked by a reversal in the flow direction. At shallower depths (e.g., $z = 6{,}000$ m) only the magnitude of the flow velocity changes with high and low flow velocities during interglacial and glacial periods, respectively. Note the transient conditions during glacial periods and the abrupt change to steady single-pass flow during interglacial periods. (b) Temperature evolution at $x = 250$ and 265 m below the surface showing a somewhat delayed, gradual temperature decrease during periods of glaciation. The fast recovery of the temperature at the onset of interglacial periods indicates flushing of relatively hot water from the deep fault. The amplitude of local temperature fluctuations increases with the duration of glacial/interglacial periods.

Monitoring the temperature at the same point as in Section 4.2.1 ($x = 250$ m, 265 m below the surface) shows that the effect of these alternating flow conditions on the local temperature becomes stronger with the duration of glacial and interglacial periods. For a fault permeability of 1e-15 m^2 the temperature decreases by about 0.7°C during a glacial interval lasting 10,000 years (Figure 7b). The temperature decreases gradually after a short initial increase that is probably related to the growing convection cell at depth and upward deflection of the single-pass fluid pathways. During interglacial periods the temperature at the monitoring point recovers to 2°C above conductive conditions, corresponding to steady state conditions (Section 4.2.1), after about 10,000 years. The onset of excess recharge and deep single-pass flow at the beginning of interglacial periods flushes relatively hot water from the deep fault, resulting in a steep initial increase in temperature (Figure 7b). Figures 5b and 6b suggest that these local temperature variations

following transient recharge conditions become much more pronounced with increasing fault permeability and convection-dominated heat transport, in particular in regions of strong vertical upwelling.

4.3. Topography Variants

A single elevation high in the center of the domain constitutes a groundwater divide that splits the domain into two symmetric flow systems. The extent of each flow system along the fault plane is a factor of two shorter compared to the base case. Assuming excess supply of meteoric water, a fault permeability of 1e-15 m^2 and a topographic high with $dh = 500$ m in the center of the domain results in a layered flow system exhibiting topography-driven flow and non-Rayleigh convection in the shallow and deep fault, respectively, on either side of the groundwater divide (Figure 8a). Thus, a layered flow system is established despite excess meteoric water. The reason for this is that by shortening the extent of the flow system, infiltration into the fault is reduced. The effect on the flow system is the same as limiting the influx of meteoric water explicitly (Section 4.2.3).

When the fault permeability is increased to 1e-14 m^2, two symmetric single-pass systems develop on either side of the peak. Narrowing the distance between recharge and discharge sites in combination with excess recharge allows meteoric water to penetrate to the bottom of the fault, preventing the formation of convection cells (Figure 8b). This strong vertical downflow below the topographic high promotes self-channeling in the upflow zones and broadening of the recharge zone (cf. Figures 8a and 8b), thereby enhancing infiltration into the fault. Convection cells appear only when the infiltration rate is reduced to less than 0.15 m/yr.

The switch from topography-driven to non-Rayleigh convective flow has significant thermal (and possibly chemical) implications, in particular under the topographic high. It involves reversals in the flow direction and changes in local temperatures by as much as 80°C (Figure 8c). Under the topographic high, upwelling water from the convective system in the deep fault may potentially mix with downwelling meteoric water, inducing chemical disequilibrium and mineral precipitation or dissolution. However, the extent of fluid mixing is limited by the low fluxes in this part of system. A significant geochemical anomaly would require stable flow conditions over geological time scales.

Two topographic highs along the surface with a steep valley between (Figure 4a) further shortens the distance between recharge and discharge sites. Using a permeability of 1e-15 m^2, such topography results in essentially flat isotherms. This is because lateral heat conduction under short-wavelength topographic relief effectively reduces horizontal temperature gradients, approaching in the limit a conductive system with a flat surface topography and flat isotherms. As a result, buoyancy forces at depth are weakened and meteoric water penetrates from the surface to the bottom of the fault by gravity, albeit at extremely low flow rates (on the order of 1e-5 m/yr under excess supply of meteoric water).

At a fault permeability of 1e-14 m^2 a stable arrangement of four convection cells is established at depth, with upflow and downflow under topographic highs and lows, respectively, confining topography-driven flow to shallow depth.

The results show that short wavelength hill-and-valley topography is not suited for establishing a deep fault-bounded single-pass flow system. With regard to the Grimsel fault, these findings are consistent with the conceptual model of deep fluid flow driven by the regional-scale (∼10 km) increase in topographic elevation toward the west, rather than by local mountain peaks along the fault trace.

4.4. Fault Geometry

The results shown in Figure 8a suggest that even under excess supply of meteoric water a mixed convective system can evolve if the infiltration rate into the fault is limited by the size of the recharge zone. The base case model (Figure 5a) was used to test the general validity of this assessment. The length of the fault plane was shortened while the depth of the fault plane was kept unchanged. Simulations confirm that by shortening the length of the fault plane, the depth of meteoric infiltration and topographically driven flow decrease. Using an aspect ratio of length/depth ≈1 (assuming a uniform depth of the fault of 12.5 km) and a permeability of 1e-15 m^2, meteoric water no longer reaches the bottom of the fault plane. A flat convection cell forms in the deep fault and the same hydrodynamic layering evolves as under recharge-limited conditions

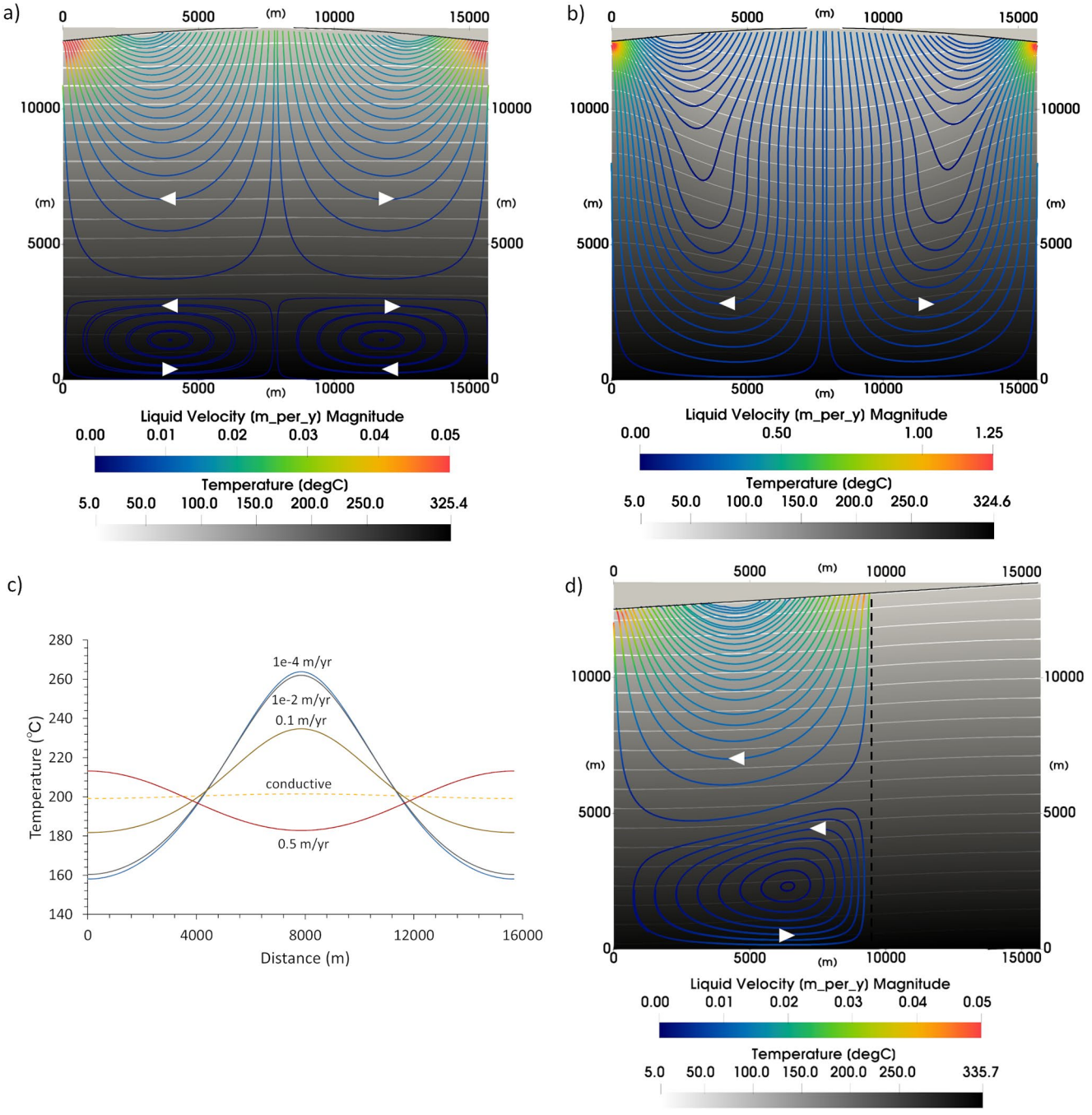

Figure 8. (a) Flow pattern for a central topographic high (dh = 500 m) with a fault permeability of 1e-15 m^2 and excess supply of meteoric recharge. Two single-pass flow systems, one on each side of the elevation high, are underlain by two convection cells in the deep fault. (b) Increasing the fault permeability to 1e-14 m^2 results in two single-pass flow systems. A strong vertical flow component causes meteoric water to penetrate to the bottom of the fault plane. (c) Horizontal temperature profiles 5,000 m above bottom of the domain as a function of the infiltration rate. The change from single-pass forced flow in the case of excess recharge (b) to convection following a decrease in meteoric recharge may reverse the flow direction and change local temperatures by as much as 80°C. (d) A lower aspect ratio of the fault plane decreases the depth of single-pass flow and establishes deep convective circulation. The aspect ratio of the hydraulically active fault plane, assuming a uniform depth of 12.5 km, is 0.75. The depth of single-pass flow varies along the plane. On average, the ratio of the fault length to the depth of single-pass flow is slightly higher than unity.

(Figure 8d). Reducing the fault length further expands the convection cell and confines single-pass groundwater flow to shallower depths. Figure 8d shows that the vertical extent and hence the depth of single-pass flow changes along the fault. A vertical profile of flow velocities indicates that the transition between single-pass flow and convection is smooth and continuous, hence there is no well-defined boundary between the two flow regimes. Nevertheless, it is possible to derive a rough estimate for the depth of single-pass flow and set it in relation to the length of the hydraulically active fault plane. This ratio of fault length to the estimated depth of single-pass flow is slightly higher than unity (~1.1 on average). A similar behavior, but involving more vigorous flow and larger convection cells for the same aspect ratio of the fault plane, can be observed at a fault permeability of 1e-14 m^2. The results suggest that there is a permeability-dependent critical aspect ratio below which a layered flow system evolves. If we consider 1e-15 m^2 to be the lowest realistic permeability of the Grimsel fault, a conservative estimate of this critical aspect ratio is around unity. This implies that, since the independently determined depth of single-pass flow in the Grimsel fault is 10 km (Diamond et al., 2018), the hydraulically connected segment of the Grimsel fault plane has to extend at least 10 km toward the west into higher terrain.

5. Discussion

Simulation results suggest that without heterogeneous permeability in the fault zone, deep single-pass flow through the Grimsel fault is possible when topography-driven flow outweighs buoyancy forces. This is the case at conditions at or below the critical Rayleigh number, which constrains the upper limit of fault permeability to be around 1e-14 m^2.

This limit is about two orders of magnitude lower than the fault permeability used in López and Smith (1995) to achieve steady convection in a fault plane. This difference is probably related to the smaller dimensions of their fault plane in terms of depth and width (2,300 and 10 m, respectively). The authors showed that the lowest permeability needed for the onset of steady convection decreases with increasing fault width and depth. Concerning the width of the fault plane, López and Smith (1995) argue that equivalent behavior is observed for two fault zones with differing permeability k but the same "transmissivity," that is, an equivalent permeability k' scaled by the fault width b according to $k' = k \times 10/b$. Based on their insight, one could predict that solely by decreasing the fault width from 100 m used in our model to 10 m used in their model, the critical permeability for the onset of convection would increase by about one order of magnitude.

The permeability limit for the onset of convection in our model is more in accord with the study by Taillefer et al. (2017, 2018), which likewise reported slightly subcritical conditions and an estimated bulk permeability of 1e-14 m^2 for two 100 m wide fault zones in a numerical study of the orogenic geothermal system in the Tet valley of the Pyrenees. The permeability of the fault was constrained by using chemical and thermal data from the thermal springs as calibration targets. A lower limit of the permeability of the Grimsel fault can similarly be derived by calibrating the model against mass and thermal fluxes discharging at Grimsel Pass. This requires extension of the model presented here and is the subject of an ongoing study. Preliminary results suggest the lower permeability limit of the Grimsel fault to be around 1e-15 m^2.

In subcritical systems two possible flow modes exist: topographically driven flow and non-Rayleigh convection. The forces driving these two modes, head gradients and lateral temperature gradients, tend to operate in opposite directions. Non-Rayleigh convection is always weak and flow rates are less than a few cm/yr. It is therefore easily overwhelmed by topography-driven flow, in particular at shallow depth. With increasing depth the hydraulic gradient driving single-pass flow decreases, such that at some critical depth non-Rayleigh convection may become dominant. A layered flow system evolves in which deep convective circulation is overlain by single-pass, topography-driven flow.

The depth of the interface between single-pass and convective flow depends on the rate of meteoric recharge. Meteoric infiltration is controlled by (a) the supply of meteoric recharge (rainfall or meltwater), (b) the hydraulic properties of the recharge zone, and (c) the cross-sectional area of the recharge zone. The effects of the hydraulic properties of the recharge zone were not considered in this study, but it is reasonable to assume that reducing the permeability of the recharge zone (e.g., due to water-rock reactions or tectonic activity) has the same effect as reducing the supply of meteoric recharge. Simulations show that if the infiltration rate falls below a certain threshold, a previously stable single-pass system collapses into

a layered flow system. In the base case simulation with a fault permeability of 1e-15 m^2 this infiltration threshold amounts to about 0.016 m/yr. Under current climatic conditions the annual rainfall at Grimsel Pass is around 2 m/yr. It is therefore reasonable to assume that the infiltration threshold is exceeded. This finding supports the initial presumption that under present conditions the Grimsel fault constitutes a single-pass flow system.

The cross-sectional area of the recharge zone may limit infiltration and induce deep convective circulation if the fault plane exhibits a low-aspect ratio (length/depth). Assuming a bulk fault permeability of 1e-15 m^2, a topographic gradient of 6.4e-2 and excess recharge for the current Grimsel system, simulations show that an aspect ratio at and below unity leads to a layered flow system with deep convective circulation in the fault plane. The inference of single-pass flow to a depth of at least 10 km implies that the hydraulically connected segment of the Grimsel fault extends at least 10 km from the discharge site on the mountain pass to a high recharge zone in the west.

At a permeability of 1e-14 m^2 and conditions near the critical Rayleigh number, mixed flow systems evolve in which free convection co-exists with single-pass flow. Although single-pass flow is still possible, heat transport and the flow pattern are affected by buoyancy forces, as evidenced by sloping isotherms and a relatively strong vertical flow component, respectively (e.g., Figure 6d). Enhanced vertical flow increases the thermal output and strengthens the chemical signature of deep water–rock interaction in the water discharging at the surface. At even higher permeabilities (>1e-13 m^2) free convection completely overwhelms other modes of flow.

The Grimsel system is known to have been active at least since 3.3 Ma and the residence time of the currently discharging thermal water is known to be at least 30,000 years. Given the quick response of hydraulic conditions to changes in recharge conditions at the surface (Figure 7a), the depth of fluid circulation may have changed repeatedly throughout the Pleistocene. Deep convective circulation in isolated convection cells may have alternated with deep single-pass flow during glacial and interglacial periods, respectively. Thus it is possible that the hydrothermal water discharging at the spring today was trapped in deep convective circulation during the last glaciation event which began about 30,000 years ago. Infiltration of this water must have occurred prior to this last glaciation event, rendering the water older than 30,000 years, consistent with observations.

6. Conclusions

The simulations presented here reveal how variable recharge conditions drive fault-hosted orogenic geothermal systems subject to alternating glacial and interglacial climate events. This provides a framework for future modeling to evaluate other important aspects of these dynamic flow systems, such as the role of heterogeneous permeability and the possibility of flow channeling.

Our modeling results underscore how fault-bounded flow in amagmatic mountainous terrains is controlled by two competing forces: gravity and buoyancy. Gravity-induced flow occurs from topographic highs to lows, and buoyancy-driven flow is caused by instabilities when the system-specific critical Rayleigh number is exceeded, or when lateral temperature gradients under topographic relief induce slow background flow at subcritical Rayleigh numbers (i.e., non-Rayleigh convection). Thus, at subcritical conditions and with zero recharge, groundwater in mountainous terrain will never be motionless, although lateral conduction under short wavelength hill-and-valley topography may flatten isotherms thereby reducing the driving force for non-Rayleigh convection.

The implications of the results for the Grimsel Pass system are that deep (~10 km) infiltration into the Grimsel fault can occur because of abundant meteoric recharge and because the hydraulically conductive fault extends far (≥10 km) into increasingly higher mountainous terrain toward the west. Along the Grimsel fault, it is likely that repeated glaciation/interglacial periods and transient recharge conditions led to changing flow modes during the Pleistocene. At Grimsel and in similar orogenic systems, such changes should be considered in the interpretation of geochemical data used to estimate fluid residence times, mixing ratios and the depth of meteoric infiltration.

Data Availability Statement

The data on which the simulations based are available through Waber et al. (2017), Diamond et al. (2018), and Wanner et al. (2019). An annotated input file and data sets needed to run the base case simulation can be downloaded at https://doi.org/10.5281/zenodo.4191747.

Acknowledgments
We thank the Swiss Competence Center for Energy Research-Supply of Electricity (SCCER-SoE) for their support of geothermal research at the University of Bern. Support is also acknowledged from National Research Programme NRP 70 "Energy Turnaround" funded by Swiss National Science Foundation (SNF) grant 407040_153889 to L.W. Diamond. The authors thank Steven Ingebritsen and one anonymous reviewer for providing helpful comments that improved the manuscript.

References

Alt-Epping, P., & Zhao, C. (2010). Reactive mass transport modelling of a three-dimensional vertical fault zone with a finger-like convective flow regime. *Journal of Geochemical Exploration*, *106*(1–3), 8–23.

Anderson, D. M., & Morgenstern, N. R. (1973). *Physics, chemistry, and mechanics of frozen ground: A review* (pp. 257–288). Washington: Second International Conference on Permafrost, National Academy of Sciences.

Anderson, D. M., & Tice, A. R. (1972). Predicting unfrozen water contents in frozen soils from surface area measurements. *Highway Research Record*, *393*, 12–18.

Belgrano, T. M., Herwegh, M., & Berger, A. (2016). Inherited structural controls on fault geometry, architecture and hydrothermal activity: An example from Grimsel Pass, Switzerland. *Swiss Journal of Geosciences*, *109*(3), 345–364.

Bickle, M. J., & McKenzie, D. (1987). The transport of heat and matter by fluids during metamorphism. *Contributions to Mineralogy and Petrology*, *95*, 384–392. https://doi.org/10.1007/bf00371852

Bossart, P., & Mazurek, M. (1991). *Grimsel test site structural geology and water flow-paths in the migration shear zone Nagra technical report NTB* (Vol. 91–12, pp. 1–55). Wettingen: Nagra.

Craw, D., Koons, P. O., Zeitler, P. K., & Kidd, W. S. F. (2005). Fluid evolution and thermal structure in the rapidly exhuming gneiss complex of Namche Barwa–Gyala Peri, eastern Himalayan syntaxis. *Journal of Metamorphic Geology*, *23*, 829–845.

Cserepes, L., & Lenkey, L. (2004). Forms of hydrothermal and hydraulic flow in a homo-geneous unconfined aquifer. *Geophysical Journal International*, *158*(2), 785–797. https://doi.org/10.1111/j.1365-246X.2004.02182.x

Diamond, L. W., Wanner, C., & Waber, H. N. (2018). Penetration depth of meteoric water in orogenic geothermal systems. *Geology*, *46*, 1063–1066. https://doi.org/10.1130/g45394.1

Dillon, H. B., & Andersland, O. B. (1966). Predicting unfrozen water contents in Frozen Soils. *Canadian Geotechnical Journal*, *3*(2), 53–60. https://doi.org/10.1139/t66-007

Dzikowski, M., Josnin, J. Y., & Roche, N. (2016). Thermal influence of an alpine deep hydrothermal fault on the surrounding rocks. *Groundwater*, *54*, 55–65.

Elder, J. W. (1967). Transient convection in a porous medium. *Journal of Fluid Mechanics*, *27*(3), 609–623.

Fisher, A. T., Becker, K., Narasimhan, T. N., Langseth, M. G., & Mottl, M. J. (1990). Passive, off-axis convection through the southern flank of the Costa Rica Rift. *Journal of Geophysical Research*, *95*, 9343–9370. https://doi.org/10.1029/jb095ib06p09343

Forster, C. B., & Smith, L. (1988a). Groundwater flow systems in mountainous terrain. 1. Numerical modeling techniques. *Water Resources Research*, *24*, 999–1010. https://doi.org/10.1029/wr024i007p00999

Forster, C. B., & Smith, L. (1988b). Groundwater flow systems in mountainous terrain, 2, Controlling factors. *Water Resources Research*, *24*, 1011–1023. https://doi.org/10.1029/wr024i007p01011

Forster, C. B., & Smith, L. (1989). The influence of groundwater flow on thermal regimes in mountainous terrain: A model study. *Journal of Geophysical Research*, *94*(B7), 9439–9451. https://doi.org/10.1029/jb094ib07p09439

Grasby, S. E., Ferguson, G., Brady, A., Sharp, C., Dunfield, P., & McMechan, M. (2016). Deep groundwater circulation and associated methane leakage in the northern Canadian Rocky Mountains. *Applied Geochemistry*, *68*, 10–18. https://doi.org/10.1016/j.apgeochem.2016.03.004

Grasby, S. E., & Hutcheon, I. (2001). Controls on the distribution of thermal springs in the southern Canadian Cordillera. *Canadian Journal of Earth Sciences*, *38*, 427–440. https://doi.org/10.1139/e00-091

Hammond, G. E., & Lichtner, P. C. (2010). Field-scale model for the natural attenuation of uranium at the Hanford 300 Area using high performance computing. *Water Resources Research*, *46*, W09527. https://doi.org/10.1029/2009WR008819

Hammond, G. E., Lichtner, P. C., & Mills, R. T. (2014). Evaluating the performance of parallel subsurface simulators: An illustrative example with PFLOTRAN. *Water Resources Research*, *50*, 208–228. https://doi.org/10.1002/2012WR013483

Hochstein, M. P., & Yang, Z. (1995). The Himalayan geothermal belt (Kashmir, Tibet, West Yunnan). In M. L. Gupta, & M. Yamano (Eds.), *Terrestrial heat flow in geothermal energy in Asia* (pp. 331–368). New Delhi: Oxford and IBH Publishing.

Hofmann, B. A., Helfer, M., Diamond, L. W., Villa, I. M., Frei, R., & Eikenberg, J. (2004). Topography-driven hydrothermal breccia mineralization of Pliocene age at Grimsel Pass, Aar massif, Central Swiss Alps. *Schweizerische Mineralogische und Petrographische Mitteilungen*, *84*, 271–302.

Ingebritsen, S. E., Sanford, W. E., & Neuzil, C. E. (2006). *Groundwater in geologic processes* (2nd ed., p. 536). Cambridge: Cambridge University Press.

Kleinberg, R. L., & Griffin, D. D. (2005). NMR measurements of permafrost: Unfrozen water assay, pore-scale distribution of ice, and hydraulic permeability of sediments. *Cold Regions Science and Technology*, *42*(1), 63–77. https://doi.org/10.1016/j.coldregions.2004.12.002

Lapwood, E. R. (1948). Convection of a fluid in a porous medium. *Proceedings of the Cambridge Philosophical Society*, *44*, 508–521. https://doi.org/10.1017/s030500410002452x

López, D. L., & Smith, L. (1995). Fluid flow in fault zones: Analysis of the interplay of convective circulation and topographically driven groundwater flow. *Water Resources Research*, *31*(6), 1489–1503. https://doi.org/10.1029/95wr00422

Magri, F., Möller, S., Inbar, N., Möller, P., Raggad, M., Rödiger, T., et al. (2016). 2d and 3d coexisting modes of thermal convection in fractured hydrothermal systems–Implications for transboundary flow in the lower Yarmouk gorge. *Marine and Petroleum Geology*, *78*, 750–758. https://doi.org/10.1016/j.marpetgeo.2016.10.002

Mailloux, B., Person, M., Strayer, P., Hudleston, P. J., Cather, S., Dunbar, N., & Hudleston, P. (1999). Tectonic and stratigraphic controls on the hydrothermal evolution of the Rio Grande Rift. *Water Resources Research*, *35*(9), 2641–2659. https://doi.org/10.1029/1999wr900110

Manga, M., & Kirchner, J. W. (2004). Interpreting the temperature of water at cold springs and the importance of gravitational potential energy. *Water Resources Research*, *40*, W05110. https://doi.org/10.1029/2003WR002905

Manning, C. E., & Ingebritsen, S. E. (1999). Permeability of the continental crust: The implications of geothermal data and metamorphic systems. *Reviews of Geophysics*, *37*, 127–150. https://doi.org/10.1029/1998rg900002

Maréchal, J. C., Perrochet, P., & Tacher, L. (1999). Long-term simulations of thermal and hydraulic characteristics in a mountain massif: The Mont Blanc case study, French, and Italian Alps. *Hydrogeology Journal*, *7*, 341–354. https://doi.org/10.1007/s100400050207

Menzies, C. D., Teagle, D. A. H., Craw, D., Cox, S. C., Boyce, A. J., Barrie, C. D., & Roberts, S. (2014). Incursion of meteoric waters into the ductile regime in an active orogen. *Earth and Planetary Science Letters*, *399*, 1–13. https://doi.org/10.1016/j.epsl.2014.04.046

Murphy, D. H. (1979). Convective instabilities in vertical fractures and faults. *Journal of Geophysical Research*, *84*, 6121–6130. https://doi.org/10.1029/jb084ib11p06121

Noetzli, J., & Phillips, M. (2019). *Mountain permafrost hydrology. Hydro-CH2018 Project* (p. 18). Switzerland: Comissioned by the Federal Office for the Environment (FOEN), Bern. https://doi.org/10.16904/slf.1

Norton, D., & Knight, J. (1977). Transport phenomena in hydrothermal systems: Cooling plutons. *American Journal of Science*, *277*, 937–981. https://doi.org/10.2475/ajs.277.8.937

Ota, K., Möri, A., Alexander, W. R., Frieg, B., & Schild, M. (2003). Influence of the mode of matrix porosity determination on matrix diffusion calculations. *Journal of Contaminant Hydrology*, *61*(1–4), 131–145. https://doi.org/10.1016/s0169-7722(02)00139-0

Pepin, J., Person, M., Phillips, F., Kelley, S., Timmons, S., Witcher, J., et al. (2014). Deep fluid circulation within crystalline basement rocks and the role of hydrologic windows in the formation of the truth or consequences, New Mexico low-temperature geothermal system. *Geofluids*, *15*, 139–160. https://doi.org/10.1111/gfl.12111

Pfeifer, H. R., Sanchez, A., & Degueldre, C. (1992). Thermal springs in granitic rocks from the Grimsel Pass (Swiss Alps): The late stage of a hydrothermal system related to Alpine Orogeny. In Y. K. Kharaka, & A. S. Maest (Eds.), *Proceedings of water-rock interaction WRI–7. A.A.*

Preusser, F., Graf, H. R., Keller, O., Kryss, E., & Schlüchter, C. (2011). Quaternary glaciation history of northern Switzerland. *Quaternary Science Journal*, *60*(2–3), 282–305. https://doi.org/10.3285/eg.60.2-3.06

Raffensperger, J., & Vlassopoulos, D. (1999). The potential for free and mixed convection insedimentary basins. *Hydrogeology Journal*, *7*(6), 505–520. https://doi.org/10.1007/s100400050224

Reyes, A. G. (2015). Low-temperature geothermal reserves in New Zealand. *Geothermics*, *56*, 138–161. https://doi.org/10.1016/j.geothermics.2015.04.004

Reyes, A. G., Christenson, B. W., & Faure, K. (2010). Sources of solutes and heat in low-enthalpy mineral waters and their relation to tectonic setting, New Zealand. *Journal of Volcanology and Geothermal Research*, *192*, 117–141. https://doi.org/10.1016/j.jvolgeores.2010.02.015

Simms, M. A., & Garven, G. (2004). Thermal convection in faulted extensional sedimentary basins: Theoretical results from finite-element modeling. *Geofluids*, *4*, 109–130. https://doi.org/10.1111/j.1468-8115.2004.00069.x

Smith, L., & Chapman, D. S. (1985). The influence of water table configuration on the near-surface thermal regime. *Journal of Geodynamics*, *4*, 183–198. https://doi.org/10.1016/0264-3707(85)90059-6

Sonney, R., & Vuataz, F.-D. (2008). Properties of geothermal fluids in Switzerland: A new interactive database. *Geothermics*, *37*, 496–509. https://doi.org/10.1016/j.geothermics.2008.07.001

Sonney, R., & Vuataz, F.-D. (2009). Numerical modelling of Alpine deep flow systems: A management and prediction tool for an exploited geothermal reservoir (Lavey-les-Bains, Switzerland). *Hydrogeology Journal*, *17*, 601–616. https://doi.org/10.1007/s10040-008-0394-y

Sonney, R., & Vuataz, F.-D. (2010). Remobilisation of deep Na-Cl waters by a regional flow system in the Alps: Case study of Saint-Gervais-les-Bains (France). *Comptes Rendus Geoscience*, *342*, 151–161. https://doi.org/10.1016/j.crte.2009.12.011

Stober, I., Zhong, J., Zhang, L., & Bucher, K. (2016). Deep hydrothermal fluid–rock interaction: The thermal springs of Da Qaidam, China. *Geofluids*, *16*(4), 711–728. https://doi.org/10.1111/gfl.12190

Stöckhert, B., Brix, M. R., Kleinschrodt, R., Hurford, A. J., & Wirth, R. (1999). Thermochronometry and microstructures of quartz–A comparison with experimental flow laws and predictions on the temperature of the brittle–plastic transition. *Journal of Structural Geology*, *21*, 351–369. https://doi.org/10.1016/s0191-8141(98)00114-x

Szijárto, M., Galsa, A., Tóth, Á., & Mádl-Szönyi, J. (2019). Numerical investigation of the combined effect of forced and free thermal convection in synthetic groundwater basins. *Journal of Hydrology*, *572*, 364–379. https://doi.org/10.1016/j.jhydrol.2019.03.003

Taillefer, A., Guillou-Frottier, L., Soliva, R., Magri, F., Lopez, S., Courrioux, G., et al. (2018). Topographic and faults control of hydrothermal circulation along dormant faults in an orogen. *Geochemistry, Geophysics, Geosystems*, *19*(12), 4972–4995. https://doi.org/10.1029/2018gc007965

Taillefer, A., Soliva, R., Guillou-frottier, L., Le Goff, E., Martin, G., & Seranne, M. (2017). Fault-related controls on upward hydrothermal flow; an integrated geological study of the Têt fault, eastern Pyrénées (France). *Geofluids*, *19*, 8190109.

Thiebaud, E., Gallino, S. P., Dzikowski, M., & Gasquet, D. (2010). The influence of glaciations on the dynamics of mountain hydrothermal systems: Numerical modeling of the LaLéchère system (Savoie, France). *Bulletin de la Societe Geologique de France*, *181*, 295–304. https://doi.org/10.2113/gssgfbull.181.4.295

Tóth, J. (2009). *Gravitational systems of groundwater flow: Theory, evaluation, utilization* (p. 297). Cambridge: Cambridge University Press.

Upton, P., Craw, D., Yu, B., & Chen, Y.-G. (2011). Controls on fluid flow in transpressive orogens, Taiwan and New Zealand. *Geological Society, London, Special Publications*, *359*, 249–265. https://doi.org/10.1144/sp359.14

Vernon, A. J., van der Beek, P. A., Sinclair, H. D., & Rahn, M. K. (2008). Increase in late Neogene denudation of the European Alps confirmed by analysis of a fission-track thermochronology database. *Earth and Planetary Science Letters*, *270*(3–4), 316–329. https://doi.org/10.1016/j.epsl.2008.03.053

Waber, H. N., Schneeberger, R., Mäder, U. K., & Wanner, C. (2017). Constraints on evolution and residence time of geothermal water in granitic rocks at Grimsel (Switzerland). *Procedia Earth and Planetary Science*, *17*, 774–777. https://doi.org/10.1016/j.proeps.2017.01.026

Wangen, M. (1997). Non-Rayleigh convection caused by ground surface topography. *Transport in Porous Media*, *26*, 299–318. https://doi.org/10.1023/a:1006570819908

Wanner, C., Diamond, L. W., & Alt-Epping, P. (2019). Quantification of deep 3D thermal anomalies in orogenic geothermal systems from surface observations: Implications for heat exploration and thermochronology. *Journal of Geophysical Research*, *124*(11), 10839–10854. https://doi.org/10.1029/2019jb018335

Wanner, C., Pöthig, R., Carrero, S., Fernandez-Martinez, A., Jäger, C., & Furrer, G. (2018). Natural occurrence of nanocrystalline Al-hydroxysulfates: Insights on formation, Al solubility control and as retention. *Geochimica et Cosmochimica Acta*, *238*, 252–269. https://doi.org/10.1016/j.gca.2018.06.031

Wanner, C., Waber, H. N., & Bucher, K. (2020). Geochemical evidence for regional and long-term topography-driven groundwater flow in an orogenic crystalline basement (Aar Massif, Switzerland). *Journal of Hydrology*, *581*, 124374. https://doi.org/10.1016/j.jhydrol.2019.124374

Yang, J., Large, R. R., & Bull, S. W. (2004). Factors controlling free thermal convection in faults in sedimentary basins: Implications for the formation of zinc-lead mineral deposits. *Geofluids*, *4*(3), 237–247. https://doi.org/10.1111/j.1468-8123.2004.00084.x

Yang, J. W., Feng, Z. H., Luo, X. R., & Chen, Y. R. (2010). Numerically quantifying the relative importance of topography and buoyancy in driving groundwater flow. *Science in China - Series D: Earth Sciences*, *53*(1), 64–71. https://doi.org/10.1007/s11430-009-0185-x

Zhao, C., Hobbs, B. E., Mühlhaus, H. B., Ord, A., & Lin, G. (2003). Convective instability of 3-D fluid-saturated geological fault zones heated from below. *Geophysical Journal*, *155*(1), 213–220. https://doi.org/10.1046/j.1365-246x.2003.02032.x